First observations of polarized scattering over ice clouds at close-to-millimeter wavelengths (157GHz) with MADRAS on board the Megha-Tropiques mission

Eric Defer, Victoria Galligani, Catherine Prigent, and Carlos Jimenez

LERMA – CNRS/Observatoire de Paris

V3.1

Corresponding Author: Eric Defer

eric.defer@obspm.fr

LERMA – CNRS/Observatoire de Paris

61 avenue de l'Observatoire

75014 Paris

France

Phone :   +33 1 40 51 2135

Fax :   +33 1 40 51 2002

Abstract

Polarized scattering by frozen hydrometeors is investigated for the first time up to 157 GHz, based on the passive microwave observations of the Microwave Analysis and Detection of Rain and Atmospheric Structures (MADRAS) instrument on board the Indo-French Megha-Tropiques satellite mission. A comparison with time-coincident Tropical Rainfall Measurement Mission (TRMM) Microwave Imager (TMI) records confirms the consistency of the coincident observations collected independently by the two instruments up to 89 GHz. The MADRAS noise levels of 1.2 K at 89 GHz and of 2.5 K at 157 GHz are in agreement with the required specifications of the mission. Compared to the 89 GHz polarized channels that mainly sense large ice particles (snow and graupel), the 157 GHz polarized channel is sensitive to smaller particles and provides additional information on the cloud systems. The analysis of the radiometric signal at 157 GHz reveals that the ice scattering can induce a polarization difference of the order of 10 K at that frequency. Based on radiative transfer modelling the specific signature is interpreted as the effect of mainly horizontally oriented ice cloud particles. This suggests that the effects of the cloud particle orientation should be considered in rain and cloud retrievals using passive radiometry at microwave and millimetre wavelengths.

Key points

1 - Cloud scattering induces polarization difference of the order of 10K at 157GHz

2 - Particle orientation must be considered in rain and cloud microwave retrievals

3 - MADRAS radiometric sensitivities at 89 GHz and 157 GHz are below 1.2 K and 2.5 K

Index Terms and keywords

1) Remote sensing

2) Radiative processes

3) Clouds and aerosols

Introduction

  Satellite observations from the visible to the microwaves are used operationally by the weather centers for the characterization of cloud and rain. Passive microwaves are recognized to provide unique information about the hydrometeors, with their ability to penetrate the cloud structure whereas infrared and visible observations from satellite usually provides properties of the top of clouds like cloud top height or cloud top phase (e.g. Stubenrauch et al., 2013). Satellite remote sensing at millimeter waves has been proven recently to show a high sensitivity to the cloud ice phase due to the strong scattering signal from the frozen particles at these wavelengths [Evans et al., 2005; Buehler et al., 2007; Jimenez et al., 2007; Defer et al., 2008]. This influenced the recent decision of having an Ice Cloud Imager (ICI) at frequencies between 170 and 670 GHz on board the next generation of operational satellites in Europe (MetOp-SG). The MetOP-SG mission will also carry the MicroWave Imager (MWI) and the MicroWave Sounder (MWS), both operating at lower frequencies than ICI.

  At low microwave frequencies (roughly below 60 GHz) microwave radiation is essentially sensitive to the emission from liquid clouds. At higher frequencies, scattering processes also take place and can provide additional information on the cloud ice phase. Changing the observation frequency will change the observed brightness temperature (TB) signal of the Earth's upwelling radiation via changes in the sensitivity to the interaction mechanisms. At high microwave frequencies the scattering by frozen hydrometeors increases and can depress the TB signal. This reduction in the observed TB signal can be used to detect and quantify ice and snow clouds in the microwave range as demonstrated for rain identification with scattering index (Grody, 1991).

  Within this framework, understanding and quantifying the scattering signals from frozen clouds, and more generally the frozen phase, at millimeter waves are a necessity for an

optimal retrieval of the ice cloud characteristics from the future satellite measurements. The interaction of millimeter radiation with frozen hydrometeors is complex and involves not only the ice quantities but also the size distribution of the particles, their dielectric properties, their shapes, and their orientation.

Polarized scattering signals from the frozen phase have been evidenced up to 90 GHz, from measurements with conical scanners such as the Special Sensor Microwave Imager (SSM/I) or Tropical Rainfall Measurement Mission (TRMM) Microwave Imager (TMI) [Prigent et al., 2001, 2005; Galligani et al., 2013]. It has been shown that this polarized scattering can be explained by the interaction of the radiation with non-spherical and oriented particles and can bring insight into the cloud microphysics. Up to recently, space-based polarized measurements over 90 GHz were not available. Current meteorological satellite observations are provided up to 190 GHz, but in cross track mode without separate measurements of the two orthogonal polarized signals.

Recently new space-based observations at 157 GHz along the two orthogonal polarizations have been performed thanks to the Megha-Tropiques (MT) mission. The MT mission [Desbois et al., 2007] is a collaborative satellite project, developed by ISRO (Indian Space Research Organization) and CNES (Centre National d'Etudes Spatiales). The Indo-French satellite, launched in 2011, carries several instruments, including a microwave imager MADRAS (Microwave Analysis and Detection of Rain and Atmospheric Structures) and a microwave sounder SAPHIR (Sondeur Atmosphérique du Profil d'Humidité Intertropicale par Radiométrie). MADRAS is a conical scanner with frequencies between 19 and 157 GHz. Both orthogonal polarizations are measured for most frequencies, including at 157 GHz. In this study, space-based polarized scattering signals over ice clouds are observed and analyzed for the first time at a frequency above 100 GHz, where the sensitivity to cloud ice scattering is expected to be higher.

The MADRAS instrument is briefly described, insisting on the sensitivity of the high frequency channels (section 1). The observed polarized scattering over ice clouds is then analyzed with special attention to its frequency dependence (section 2). Radiative transfer (RT) simulations help interpret the observations (section 3). Section 4 concludes this study.

1. MADRAS on board Megha-Tropiques

The objective of the MT mission is to study the water cycle in the intertropical region, and to evaluate its influence on the energy budget [Desbois et al., 2007]. The MT satellite was successfully launched by ISRO from the Sriharikota launch pad (India) and put on a circular orbit at 865 km, inclined by 20° to the equator. Thanks to this low inclined orbit, MT is providing frequent observations over the tropics, between latitudes of +/-23° and is part of the Global Precipitation Mission (GPM) constellation. MT carries two microwave instruments: SAPHIR, a cross track humidity sounder with 6 channels around the H_2O line at 183 GHz, and a conical imager with an incidence angle of 53.5°, MADRAS, with frequencies at 18.7, 23.8, 36.5, 89 and 157 GHz for both orthogonal polarizations (except at 23.8 GHz that is vertical only) [Karouche and Raju, 2010].

MADRAS conical scan consists in 54, 214 and 356 pixels at low (18 to 36 GHz), medium (89 GHz) and high (157 GHz) frequencies respectively. To obtain the specified pixels with the required spatial resolution (Table 1) and achieve the requested radiometric sensitivity, data are over-sampled on board in the cross track direction as described in Karouche et al. (2013).

Table 1 lists the different specifications of the MADRAS instrument including the required and goal Noise Equivalent Differential Temperature (NEDT) set to 2.6 K and 2 K, respectively at 157 GHz [Goldstein and Karouche, 2013]. Analysis performed by CNES on

in-flight records indicated better sensitivity than the requirements (as listed in Table 1), with even better performances in flight compared to the assessment performed on the ground during integration at ISRO [Goldstein and Karouche, 2013]. Details on CNES flight tests and calibration as well as long term monitoring of MT payloads are available at http://smsc.cnes.fr/MEGHAT/Fr/A_recette_vol.htm.

The MADRAS V05 dataset studied here covers an observational period from 13 October 2011 to 1 February 2013. Unfortunately, due to a serious anomaly observed in the MADRAS scan mechanism, the instrument is no longer operational and does not provide data since February 2013.

2. Analysis of the MADRAS observations over ice clouds

An example of MADRAS observations is shown in Figure 1, over both ocean and land, over the south east coast of Africa, at 36, 89, and 157 GHz, for the vertical polarization (left) and for the polarization difference (right). The ocean surface emissivities are rather low and polarized, contrarily to the land that usually has high emissivities with very limited polarization signatures. For the low frequency channels, atmospheric opacity is low and therefore the contrast between ocean and land is large. At 157 GHz, the atmospheric opacity in these humid tropical regions almost completely masks the surface signal. Note the differences in spatial resolution from 36 GHz to 157 GHz (from 67 to 10 km, Table 1), with rather blurred structures at 36 GHz as compared to the higher frequencies. At 36 GHz, the liquid water emission in the clouds induces an increase of the TBs over the radiatively cold ocean but a decrease over the highly emitting land due to the colder cloud temperatures. The cloud emission also induces a decrease of the polarized surface emissions over ocean (Figure 1b). The observed large polarized signature, defined as the difference of the brightness temperature between the vertical polarization and the horizontal polarization (TBVH), over

land at 37 and 89 GHz does not correspond to cloud structures, but to water surfaces (e.g. lake Malawi between 14S-10S and 34E-35E, lake Rukwa centered on 8S and 32E, or the south part of the lake Tanganyika around 7S and 35E). At 157 GHz, some cloud structures appear cold over both ocean and land, with TBs down to 80 K (Figure 1e), which is much lower than the physical temperature of the upper part of the clouds. This is due to scattering by the cloud ice phase. The low TBs are also associated with an increase in the TB157VH polarization signal (Figure 1f). This cannot be due to the surface contribution, as the cloud free areas at 157 GHz do not show any polarization. In addition scattering from spherical particles cannot generate a polarized signal of the order of 10 K. However, as already observed close to 85 GHz, non-spherical horizontally aligned particles can generate significant positive polarized signal [Prigent et al., 2001; Prigent et al., 2005; Galligani et al., 2013]. These first polarized measurements at 157 GHz from MADRAS tend to show, and as discussed later in the paper, that polarized scattering by cloud systems is very common at 157 GHz, with larger polarization signal than at 89 GHz.

Figures 2 and 3 show almost coincident TRMM and MADRAS observations in two zones of interest of Figure 1 (TRMM observed the same region about 6 min after MT). As detailed in the Annex, the comparison of the temporally and spatially coincident brightness temperatures confirms the spatial and radiometric consistencies of the MADRAS and TMI microwave records in the common wavebands. Additional TRMM instruments are considered here: it includes the Precipitation Radar (PR) and the Visible and Infrared Scanner (VIRS) (Kummerow et al., 1998). Figure 2 focuses on deep convective clouds that exhibit significant cold TBs at 89 and 157 GHz (Figure 2a,c). Convective and stratiform cloud regions already mapped at 89 GHz are also detected at 157 GHz (Figure 2a,c). The scattering signal measured at 157 GHz also emanates from the edges of convective and stratiform clouds and from partially transparent clouds at 89 GHz (Figure 2a,c). The 157 GHz channels

therefore offer the possibility to characterize better the horizontal structure of the clouds and their inner properties at the origin of the scattering. The difference of polarization at 157 GHz tends to be of the order of 7-9 K in thick clouds and close to 0 K in convective cores that exhibit cold TBVs (figure 2d). Figure 3 zooms on another region of Figure 1 that was also sampled by TRMM PR (Figure 3f). Compared to Figure 2, the sampled clouds are less convective. The radiometric responses at 89 and 157 GHz are coherent between each other and with the IR records (Figure 3e). Except for few PR pixels, the precipitation measured along the PR swath was flagged as stratiform with the presence of bright band (not shown). The 157 GHz polarization difference exceeds 7 K in the precipitating clouds and covers a more extended area than at 89 GHz (Figure 3d,e).

The previous section focused on examples of typical radiometric signals and their characteristics at the cloud scale. In the following we summarize the main scattering features based on TBs collected over 14 days of MADRAS records selected during the studied period (i.e. 13 October 2011 to 1 February 2013) over the full tropical region covered by MADRAS. Figure 4 presents the relationship between MADRAS brightness temperature polarization differences (TBVH) and brightness temperatures in vertical polarization (TBV). These observations passed additional in-house verification simultaneously performed on the radiometric signals at 89 GHz and 157 GHz. The ocean and land cases are treated separately according to CNES surface type categorization. Due to the different sampling rates, the number of quality-controlled pixels at 157 GHz is approximately twice the number of quality-controlled pixels at lower frequencies. The emission and scattering regimes can be easily distinguished, especially over ocean. Over ocean, at 36, 89, and 157 GHz, clear sky and thin clouds have low TBV with significant polarization difference (the lower the frequency, the larger the polarization difference) but when the cloud opacity increases, TBV increases and the polarization difference decreases. At 157 GHz, even under clear sky

conditions, the opacity related to the water vapor in tropical region can be high (large TBV) and masks the polarized surface signal (low TBVH). At 89 and 157 GHz, in the presence of clouds with frozen hydrometeors, TBV decreases due to scattering by ice particles and can reach very low values.

Derived from Figure 4, Figure 5 represents the most frequent polarization difference at 89 and 157 GHz versus TBV in the scattering regime for ocean and land separately. The scattering regime was identified from a basic filtering applied on TBV and TBVH values, i.e. TBV < 260 K and ⌈TBVH⌈ < 20 K. Mean value and standard deviation of TBVH are computed as a function of TBV per bin of 1 K for any observation in the scattering regime. Ten percent of the TBV values recorded in the scattering regime are below 217 K for sea and land at 89 GHz and below 179 and 182 K over sea and land respectively at 157 GHz. In the scattering regime, for TBV decreasing, the mean polarization difference first clearly increases up to 6-7 K at 89 GHz (Figures 5a and 5b), and up to 9-10 K at 157 GHz (Figures 5c and 5d), and then decreases for TBV below 200 K. Larger standard deviations of TBVH are observed at 157 GHz compared to 89 GHz with a maximum of ~3.5 K. Figures 5a and 5b also show that colder brightness temperatures are recorded over land than over ocean, which is consistent with deeper convection over continent than over ocean. There is only 0.6 K difference at 200 K between the most probable polarization differences over ocean and land at 157 GHz. This confirms that the surface contribution to the polarization signal here is very limited, and it is likely that this difference is related to a difference in the cloud microphysics above land and ocean.

As shown in Figures 4d, 4e and 4f, the maximum of the 2D distribution over land is located at high TBV and close to 0 K polarization for all frequencies. This is expected: the land emissivity is only weakly polarized on average, and atmospheric emission processes are not polarized. At 157 GHz (Figure 4f) a significant number of pixels corresponding to high

TBV show negative polarization differences. We argue that the distribution of the polarization difference at the maximum density of points for high TBV over land can provide an estimate of the instrument noise. This is also possible at 157 GHz over ocean, due to the high atmospheric opacity at this frequency. For these conditions, the dispersion of the TBVH around the mean value (close to 0 K) is an approximation of the noise on the polarized difference σ_{V-H}. With $\sigma_{V-H}^2 = \sigma_V^2 + \sigma_H^2$ and assuming that $\sigma_V = \sigma_H$, one can deduce an estimate of the instrument noise. Figure 6 shows the histograms of the TBVH at the TB value corresponding to the maximum density of points in Figure 4. This maximum density corresponds to TBV equal to 284 and 282 K over land at 89 and 157 GHz respectively, and 283 K over ocean at 157 GHz. At 157 GHz (Figures 6b and 6c), the maximum of the distribution is at -0.6 K (resp. 0 K) over land (resp. ocean) with a standard deviation of 3.4 K (resp. 3.5 K), while at 89 GHz over land (Figure 4a), the histogram peaks at 0 K with a standard deviation of 1.7 K. From the previous equation, and assuming a standard deviation of 3.5 K, i.e. the mean of ocean and land standard deviations (Figures 6b and 6c) for the polarization difference at 157 GHz, we deduce that the instrument noise at 157 GHz is 2.5 K, whereas the instrument noise is 1.2 K at 89 GHz. These estimates are above the values provided by CNES (Table 1), but they are in agreement with the required instrument specification (9% above the required specification at 89 GHz, 4% below the required specification at 157 GHz).

3. Confirmation of the interpretation of the polarized scattering with radiative transfer simulations

Radiative transfer simulations were performed with the Atmospheric Radiative Transfer Simulator [ARTS, Eriksson et al., 2011]. ARTS is a freely available, well documented, open source software package. ARTS handles scattering with a full and efficient account of polarization effects. It provides different methods to solve the radiative transfer

equation and the Discrete Ordinate Iterative (DOIT) method is used in this study [Emde et al., 2004]. The single scattering properties are calculated using the T-matrix code [Mishchenko, 2000] that allows the treatment of oriented spheroids. The dielectric properties of the material, the particle size distribution, their shape and orientation are all subject to large uncertainties that can translate into significant differences in terms of simulated brightness temperatures [e.g., Wiedner et al., 2004; Surussavadee and Staelin, 2006; Meirold-Mautner et al., 2007; Kulie et al., 2010]. Recently Galligani et al. [2013] used ARTS to explore the impact of changes in hydrometeor phase around the melting layer on the upwelling polarized radiation for frequencies below 100 GHz. Two different sets of simulations are performed here to explore the polarized scattering up to 157 GHz. First, simplified thermodynamic and hydrometeor profiles are used to carefully analyze the polarized radiation sensitivity to the particle characteristics (phase, size, shape, and orientation). Second, more realistic simulations of the observed signals by MADRAS are conducted by exploiting the coincidence of TMI and MADRAS observations along a transect, in the middle of the PR swath presented in Figure 3f. This allows using the profiles of water and ice species estimated from the 2A12 TMI GPROF-based product (version v7) available for that specific TRMM overpass. The focus for both simulations is on the impact of variations of the different frozen phase microphysics on the microwave polarized scattering signals observed by MADRAS.

3.1 Hydrometeor microphysical properties

The scattering properties of hydrometeors are related to their dielectric properties, their size distribution, their shape, and their orientation. For pure water, the dielectric properties are relatively easy to estimate with limited uncertainties, for instance using Liebe et al. [1991]. For pure ice, Matzler et al. [2006] model is commonly adopted, but for other frozen species, the density is a key parameter in the calculation of the dielectric properties. Mesoscale cloud models (Meso-NH for instance [Lafore et al., 1998]) usually provide the

mass content (kg/m^3) of the species per atmospheric layer and the size distribution of the

maximum dimension of the particle. However, the density and the shape of the species are

not explicitly provided by the microphysical scheme. In Meso-NH for instance, the mass of

each hydrometer category is derived from a relation of the type $m=aD^b$, with a and b

specified for each type of hydrometeor, but the shape of the particle and as a consequence its

volume and density are not explicitly given for all particles. For liquid clouds and rain, the

particles are assumed to be spheres with m proportional to D^3. Graupel and small ice crystals

are not strictly spheres ($b=2.8$ and $b=2.5$, respectively), but are approximated so in the

radiative transfer in the microwave as there is no real justification for a more complicated

treatment. Graupel species are rimmed particles for which it is reasonable to assume a

spherical shape. Small pure ice crystals can be approximated by spheres for microwave

radiative transfer calculation as their scattering is very limited. However, for snow, with m

proportional to $D^{1.9}$, the particles are clearly not spheres. For passive microwave signals, it is

viable to focus on the bulk aspect of particles as characterized by its aspect ratio, neglecting

the simulation of individual complicated particle shapes [Matrosov et al., 2005]. Aspect ratios

between 1 and 2 will be tested, and a value of 1.6 is considered realistic from aircraft

observations (Heymsfield, 2012, personal communication). The particle density for ice

crystal is that of pure ice (0.917 g/cm^3). The density of snow and graupel particles is derived

from the mass-size relationship intrinsic to the Meso-NH microphysical scheme. In terms of

dielectric properties, snow and graupel are heterogeneous media, made of ice and air (dry

snow and graupel) and possibly ice, air, and water (wet snow). The dielectric properties for

heterogeneous media can be calculated with a number of mixing formulas. The most

common, and the one used in this study, is the Maxwell-Garnett formula that gives the

effective dielectric constant of a mixture as a function of the dielectric constants of the host

material and inclusions (see applications of this formula in e.g. Battaglia et al. [2003], Olson

et al. [2001a, 2001b]). For dry snow and graupel, the host is air and the inclusion is ice. For wet snow, the Maxwell Garnett Formula is applied twice, once to calculate dry snow and a second time to mix dry snow and water.

By analyzing the scattering properties from accurate Discrete Dipole Approximation (DDA) modelling of snow particles, Liu [2004] observed that snow has scattering and absorption properties between those of a solid ice equal-mass sphere of diameter D_0 and an ice–air mixed sphere with a diameter equal to the maximum dimension of the particle D_{max}. For each frequency and particle shape, a softness parameter $SP=(D-D_0)/(D_{max}-D_0)$ is derived that gives the diameter of the best-fit equal-mass sphere. For each particle shape, this is actually equivalent to the use of a frequency dependent effective density along with modified diameters. This approach has already shown a high efficiency in reproducing real observations [Meirold-Mautner et al., 2007] and it will also be tested here.

Both randomly oriented and perfectly horizontally aligned particles are considered in our calculation. In the case of horizontally aligned particles, most particles are likely to suffer particle tumbling related to turbulence. The effect of tumbling has already been evaluated in Prigent et al. [2001]. Xie et al. [2012] showed that the simulated difference is of the order of 0.2 K in TBs between perfectly horizontally aligned particles and horizontally oriented particles with a standard deviation of 10°. We will concentrate on perfectly horizontally aligned particles for practical reasons.

3.2   Simulations with idealized profiles

These simulations involve a tropical standard atmosphere from the FASCOD (Fast Atmospheric Signature Code) database [Anderson et al., 1986], with a total column water vapor of 33 kg/m², a surface temperature of 300 K, and a land surface emissivity set to 0.9 for both polarizations (to avoid any polarized contributions from the surface itself). The

incidence angle of the simulated satellite observations is set to 53°, similar to TMI and MADRAS observation geometries. A single cloud layer (2 km thick from 6 to 8 km) is considered and populated with hydrometeors with varying Ice Water Path (IWP). A mono-disperse particle size distribution of spheroids is assumed, with radius of 50 μm to 800 μm (note that radius here refers to the radius of the sphere with equivalent mass, i.e., the effective radius).

Figure 7 presents the sensitivity of TBV and the polarization difference TBVH to the particle size at 89 and 157 GHz, for pure ice and for dry snow, for a fixed Ice Water Path (IWP) of 0.2 kg/m^2, for horizontally aligned spheroids of different aspect ratios (aspect ratio of 1 corresponds to spheres). The TBV depression is very limited at 37 GHz (not shown), even for very large particles, but strongly increases with frequencies (Figure 7a,c). TBV depression increases with particle size for dry snow and ice particles. For dry snow the scattering effect is stronger than for pure ice, because of the larger number of particles to reach the same IWP for snow than for ice (the density of ice is 0.917 g/cm^3 compared to a minimum density of 0.1 g/cm^3 for dry snow). As expected, the different aspect ratios do not have a large impact on TBV and the larger the aspect ratios produce slightly more scattering. In terms of the polarization difference, randomly oriented spheroids of aspect ratio of 1.6 or 2 produce only very limited polarized scattering signals (not shown). However, horizontally aligned spheroids, as expected, simulate significant polarization differences. The polarization difference increases with frequency (Figure 7b,d). At 157 GHz, TBVH reaches saturation around 500 μm. The different aspect ratios have a significant impact on TBVH. Note that for a realistic aspect ratio of 1.6, a polarization difference between 9 and 15 K is obtained at 157 GHz (between 4 and 7 K at 89 GHz), depending on the density of the particle (pure ice or dry snow). Such results from idealized profiles, but nonetheless realistic simulations, can explain the MADRAS observations at these two frequencies.

To further understand the MADRAS observations, Figure 8 shows the sensitivity of the polarization difference at 89 and 157 GHz to the IWP and particle radius for horizontally aligned spheroids only (aspect ratio of 1.6). Large polarization differences are simulated at 157 GHz for rather low IWP and limited radius. As observed in Figures 7 and 8, both an increase of IWC and particle size can result in the saturation of the polarization difference. This saturation is reached at lower sizes and lower IWP at 157 GHz than at 89 GHz. This saturation feature has been reported before [Miao et al., 2003; Xie and Miao, 2011] when a large number of scattering events occur. In that case, the V and H orthogonal streams of radiation tend to the same value, and their difference reaches zero.

Even though the atmospheric state was rather simplified in the simulations presented here, the sensitivity analysis reveals the impact of the microphysical properties on the polarization signal and their stronger effects with increasing frequency. The simulations so far could explain MADRAS observations, and in fact show consistency in terms of a qualitative comparison between TBV and TBVH values for 89 and 157 GHz. For example, considering particles of a specific size (450 µm) and a realistic aspect ratio (1.6), the TBVH at 157 GHz as presented in Figure 8 shows values between 10 and 15 K, while at 89 GHz TBVH is between 5 and 10 K, with TBV values at 157 GHz being considerably colder than at 89 GHz (not shown). This is in agreement with the order of magnitudes presented in Figure 5. The next section uses more realistic atmospheric parameters for the simulations and explores further the consistency of the simulations with the MADRAS observations.

3.3 Simulations with observational-based hydrometeor profiles

We focus on the system off the coast of Madagascar in Figure 3, with large TBVH differences observed by both MADRAS and TMI. The PR nadir swath crosses this system and a longitudinal transect in the middle of the PR swath is selected for our analysis of coincident MADRAS and TMI observations. The profiles of water and ice contents retrieved

from TMI (the v7 2A12 TMI product) are adopted along with coincident European Center for Medium range Weather Forecasting (ECMWF) re-analysis.

The PR 2A23 rain product [Awaka et al. 1998; Iguchi et al., 2000] provides information on the presence and location of a melting layer, on the rain type (i.e., stratiform, convective, or other), on the freezing height, and on the cloud top height, as detected by the PR. Note that the accuracy of these estimates by the PR is directly related to the PR sensitivity. The v7 TMI 2A12 based on Goddard profiling algorithm (GPROF) generates surface rainfall and vertical hydrometeor profiles of 5 species (snow cloud water, cloud liquid water, ice, graupel, and rain) from the TMI brightness temperatures. It is derived from a Bayesian retrieval and it gives the most probable structure of the hydrometeor profiles, given the TMI observations [Kummerow et al., 2011].

Figure 9 shows the measured brightness temperatures and the polarization signals recorded at 85 GHz by TMI and 89 and 157 GHz by MADRAS, along with the v7 TMI 2A12 product, for the transect of interest. Each radiometric observation located along the transect was paired to one PR beam using a minimum distance criteria. The GPROF vertical profiles (only available over ocean) map two different vertical cloud structures: C1 centred around 45.6°E (see Figure 3.b) mainly composed of snow and ice with some precipitation, and C2 from 46.5°E to 48°E with much higher hydrometeor contents and a convective tower located on the western part. This convective tower is clearly observed by TMI (Figure 9a) with a significant depression of brightness temperatures at 85 GHz. Note that the corresponding 2A12 hydrometeor content is rather limited with respect to the large TB85V TMI depression. The depression is less strong for the MADRAS 89 GHz observations due of a larger footprint, but is significant at 157 GHz along the entire transect (down to 160 K on Figure 9a). Finally the TMI depression at TB85V located around 49.2°E (Figure 9a) corresponds to deep convection: it is also observed by PR with a cloud top around 10 km (Figure 9c). Both

89 and 157 GHz MADRAS measurements show TB depressions in that part of the transect but slightly shifted in latitude and amplitude because of the observation matching methodology and the different sampling geometries for the two radiometers. Figure 9b shows an average TB157VH positive polarization signal of 10 K over C2, while at lower frequencies the polarization signal average is around 7 K. Galligani et al. [2013] reported positive polarization signal at 85 GHz in stratiform regions and in presence of bright band that can be explained by horizontally oriented hydrometeors. Finally the vertical structure of C2, as described with GPROF products, shows a vertical distribution of graupel centred mainly between 5 and 8 km (Figure 9g) while the concentration of ice particles is more pronounced above 8 km (Figure 9f). On the average, the vertically integrated snow content is more than three (ten) times higher than the vertically integrated graupel (ice) as shown in Figure 9h.

The RT calculations depend not only on the hypothesis on the microphysical properties of the hydrometeors (see sections 3.1 and 3.2) but also on the ability of the TMI 2A12 algorithm to retrieve accurate hydrometeor contents. The hydrometeor contents are provided with the TMI spatial resolution that is different from MADRAS (see Table 1). The RT simulations are conducted using realistic ocean emissivities derived from FASTEM [English and Hewison, 1998] using information on surface wind and surface skin temperature from coincident ECMWF re-analysis. As the hydrometeor contents are provided according to the highest TMI spatial resolution, simulated TBs at MADRAS frequencies are already expected to be different to the observed MADRAS TBs as the spatial resolutions are different for the two radiometers.

Figure 10a-d shows in blue the MADRAS observations along the transect of interest. Note that TMI 85 GHz observations (red lines) are also shown for reference since the v7 TMI 2A12 hydrometeor profiles are provided according to the highest TMI spatial resolution, as

mentioned earlier. Figure 10e-h summarizes the results of the sensitivity analysis to different

microphysical assumptions. Finally Figure 10i shows the vertically integrated mass content of

the different hydrometeor species as retrieved from the 2A12 algorithm along the transect of

interest. The first simulation configuration (black line) corresponds to the initially selected

parameters where the particle size distribution and the intrinsic mass for all species are

specified according to those of the microphysical scheme in the cloud mesoscale model

Meso-NH. All species, including snow, are assumed to be perfect spheres (i.e. aspect ratio of

1). The dielectric properties of the snow and graupel species retrieved from the 2A12 profiles

are calculated using the Maxwell Garnett mixing formula for dry snow with an ice volume

fraction, $f = \rho(snow)/\rho(ice)$, where $\rho(snow)$ is the density of snow and graupel as deduced

from the Meso-NH parameterization of the mass of these species. Note that the dielectric

properties are calculated for dry snow, and not for wet snow, as it is considered that the

temperatures of the snow profiles are too low to consider a wetness degree [W(%) = 0 for T <

258.15 K; W(%) = T - 258.15 for T < 258.15K; W(%) = 15 for T > 273.15 K from

Skofronick-Jackson et al. (2002)]. This configuration results in very limited scattering with

small TB depression (too warm TBV), evidenced in Figure 10e-f, and the limited

polarization, evidenced by the low positive values in TBVH in Figure 10g-h. Another

configuration where only the liquid phase is taken into account is also shown (black dotted

lines) for reference in Figure 10e-h to emphasize the importance of the scattering signal of

the ice phase at 89 and especially at 157 GHz, as discussed throughout this study.

Changing the aspect ratio, the orientation or the PSD (to that of the Meso-NH PSD

parameterization for graupel for instance for the dry snow particles), but using the same

density parameterization as given by Meso-NH does not have any impact on TBV or TBVH

(not shown). Multiplying the snow content by 1.5 in each layer decreases the simulated TBVs

at most by 5 K at 157 GHz (not shown). Snow particle sizes that are likely to scatter and

polarize the radiation at 89 and 157 GHz have very low density under the Meso-NH mass-size parameterization, affecting the dielectric properties via the ice volume fraction, and as a consequence are almost transparent to the microwaves (already seen in e.g. Meirold-Mautner et al., 2006).

Assuming the Meso-NH particle size distribution for snow species but calculating the dielectric properties for dry snow particles with a fixed density of 0.1 g/cm^3 (a value that is often selected for snow) has an important impact on the single scattering properties via the ice volume fraction and thus on the TBVs. Randomly oriented spheres result in simulated TBVs closer to those observed than the assumptions previously discussed (not shown) but do not polarize the scattering signal. In contrast, oblate horizontally oriented snow particles with an aspect ratio of 1.6 (solid red line, Figure 10e-h) lead to more realistic TBVs and polarization signals of the order of those observed by MADRAS at 157 GHz. At 89 GHz however, this assumption can generate excessive scattering (as shown here locally Figure 10e and as observed in other situations).

For the same configuration, the Meso-NH snow PSD was replaced by the Sekhon and Srivastava [1970] (SS) PSD (blue lines, Figure 10e-h), thus assuming fewer large particles and more numerous smaller ones. With the SS PSD the TBVs and TBVHs are closer to observations at 89 GHz than the previous assumption but a slight deterioration is observed at 157 GHz.

The Liu et al. (2004) parameterization of the scattering properties of snow is then tested, with the nominal PSD and density of the Meso-NH model (pink line, Figure 10e-h). It provides TBV depressions and TBVH polarizations within the observed values, without any additional fine-tuning. Finally, the sensitivity to the snow content is then analyzed by multiplying the snow content by 1.5 in each atmospheric layer for the previous configuration with Liu's approximation (green lines), configuration labelled Liu (SWCx1.5) in the

remainder of the discussion. The scattering effect is significant, especially in terms of TB depression and polarization difference at 157 GHz. The snow quantities provided by the TMI inversion are realistic, and adding more snow does not improve the agreement between simulations and observations.

A number of points from Figure 10 need to be emphasized before concluding that MADRAS observations could be explained by applying the Liu (SWCx1.5) assumptions. First of all, TBV and TBVH simulations at 89 GHz and 157 GHz are of the same order of magnitude as the observations, meaning that the assumptions are consistently constraining the RT simulations successfully. Note that the strong depression measured by TMI in Figure 10a around 46.5°W corresponds to the convective tower previously mentioned but "missed" by MADRAS mainly due to its larger footprint size. The Liu (SWCx1.5) simulation does not fully reproduce the observed strong brightness temperature depressions. This is possibly due to an underestimation of the actual hydrometeor contents from the 2A12 algorithm for that specific convective tower. In terms of the TBVH, west of 47°W, TBVH simulations are observed to peak at 85 GHz up to 13 K, in disagreement with MADRAS and TMI observations. In fact, the simulated TBVHs and TBVs are similar to MADRAS observations at clear sky conditions (e.g. west of 46.5°W). These RT simulations are clear evidence that the retrieved species contents are underestimated in this region. Otherwise, the atmosphere would be opaque enough to mask the surface emissivity polarization that is simulated at 85 GHz for TBVH for example. This is not the case for TBVH at 157 GHz since at this frequency we are not so sensitive to surface emissivity.

Considering the previous discussion, it appears that with realistic profiles and hydrometeors characteristics, and keeping in mind that there are still uncertainties on the scattering properties of the cloud microphysics, it is thus possible to explain consistently the polarized scattering signals observed at 89 and 157 GHz. This further extends the validity of

our previous interpretation of the signals up to 90 GHz, with additional stringent constraints imposed by the higher frequency.

4. Conclusion

The MADRAS instrument launched at the end of 2011 on board the Megha-Tropiques mission offers for the first time measurements of the two orthogonal polarizations at high microwave frequencies. Analysis of available quality controlled MADRAS data reveals that the radiometric sensitivity at 89 and 157 GHz are in agreement with the required instrument specifications. Further analysis of the MADRAS observations also revealed that the instrument was very stable.

We observed that at 157 GHz, scattering by clouds is polarized with TBVH larger than 8 K in 50% of the cases for TBV below 250 K, as compared to 5.5 K in 50% of the cases at 89 GHz. Simulations confirm that this is due to horizontally oriented oblate particles in the cloud frozen phase. This polarized scattering signal at 157 GHz is consistent with the polarized signatures previously observed around 85 GHz, and as expected it is more common and stronger at higher frequencies. The large occurrence of the polarized scattering in the observations as well as the magnitude of the polarization suggest that horizontally oriented oblate particles are very frequent in the cloud ice phase.

This significant polarized scattering has to be taken into account in the development of the retrieval of precipitation and cloud properties from microwave radiometry, such as the GPM algorithms that are presently under development. Especially over land, most passive microwave retrievals for precipitation are based on the scattering signal at frequencies above 80 GHz. The effect of these oriented particles has to be accounted for, at least as an additional source of noise, if not explicitly.

With the recent decision of flying an Ice Cloud Imager between 183 to 664 GHz on

board the next generation of European operational meteorological satellites, relating the observed scattering from the ice phase to accurate measurements of the cloud properties is a key challenge. The analysis of the measurements provided by MADRAS contributes to the preparation of this promising instrument, with polarimetric measurements at 170 and 670 GHz for a better description of the frozen hydrometeors.

ANNEX

Nearly-coincident MADRAS and TMI observations are available for the scene shown in Figure 1 and Figure A.1 respectively. The time difference is 6 min. Despite the different spatial resolutions and slightly different frequencies, the observations of the two radiometers are quite similar in terms of radiometric range and sensitivity over land and ocean. MADRAS measurements are very stable along a given scan, and from a scan to the next at high frequencies. No clear jump between scan lines is observed on the images of the polarization differences at 89 or 157 GHz, whereas at 85 GHz with TMI, a large noise is evident on the polarization difference maps, within a scan and from one scan to the next.

Figure A.2 shows the scatter plots of TBs and polarization differences for the common spectral bands (ocean and land together). At 35-37 GHz, the observations from the two radiometers span over the same radiometric domain even if TMI reported more convection-related scattering because of a better spatial resolution (9 km x16 km for TMI [Kummerow et al., 1998], 40 km x 67 km for MADRAS as listed in Table 1). At 85-89 GHz, even if the number of pixels from two radiometers is almost the same, more negative polarization differences are reported by TMI, while the distribution of MADRAS polarization difference at TBs lower than 200 K seems to be centered around 5 K. This pinpoints to the need for thorough investigations of the calibration of each radiometer if their observations have to be used jointly.

Figure A.3 shows the histograms and the cumulative distributions of the brightness temperatures for all surfaces together, for common radiometric band and polarization of the two radiometers. These histograms are computed from the radiometric measurements shown in Figures 1 and A.1 but for the common area defined by the intersection of MADRAS and TMI swaths. At 37 GHz, both radiometers provide rather similar histograms for both sides of the distributions (Figure A.3a,b). At 85 GHz, for both polarizations, differences exist at cold brightness temperatures, i.e. for convective clouds (Figure A.3d,e). Those discrepancies could be explained by the different spatial resolutions between the two radiometers, the viewing geometry of the convective clouds depending on the orientation of the radiometer beams relative to the cloud structure, and the natural evolution of the sampled clouds between the two overpasses (delay of 6 min). While the histograms of the polarization difference at 37 GHz are rather similar (Figure A.3c), some differences are observed at 85 GHz (Figure A.3f): TMI recorded negative-to-null polarization differences while MADRAS did not, and smaller positive difference polarizations are recorded by MADRAS. These discrepancies could be explained by the different spatial resolutions of the two radiometers and by the different radiometric sensitivities between the instruments (see Table 1 for MADRAS. TMI noise levels are 0.36 K, 0.31 K, 0.52 K and 0.93 K for 37 GHz V, 37 GHz H, 85 GHz V and 85 GHz H channels respectively [Kummerow et al., 1998]).

From these comparisons, we can conclude that MADRAS performs well, with results very similar to TMI for their common (or close) channels.

Acknowledgements.

References:

Anderson, G. P., S. Clough, F. Kneizys, J. Chetwynd, and E. P. Shettle (1986), AFGL atmospheric constituent profiles (0.120 km), Tech. rep., DTIC Document.

Awaka, J., T. Iguchi, and K. Okamoto (1998), Early results on rain type classification by the Tropical Rainfall Measuring Mission (TRMM) precipitation radar, Proc. 8th URSI Commission F Open Symp., Aveiro, Portugal, pp.143-146.

Battaglia, A., C. Kummerow, Dong-Bin Shin, and C. Williams, (2003), Constraining microwave brightness temperatures by radar bright band observations, J. Atmos. Oceanic. Technol., 20, 856–871.

Buehler, S. A. , C. Jimenez, K. F. Evans, P. Eriksson, B. Rydberg, A. J. Heymsfield, C. J. Stubenrauch, U. Lohmann, C. Emde, V. O. John, T. R. Sreerekhai and C. P. Davis (2007), A concept for a satellite mission to measure cloud ice water path, ice particle size, and

cloud altitude, Q. J. R. Meteorol. Soc., 133, 109-128.

Defer, E., C. Prigent, F. Aires, J. R. Pardo, C. J. Walden, O.-Z. Zanifé, J.-P. Chaboureau, and J.-P. Pinty (2008), Development of precipitation retrievals at millimeter and sub-millimeter wavelengths for geostationary satellites. J. Geophys. Res., 113, D08111, doi:10.1029/2007JD008673.

Desbois, M., M. Capderou, L. Eymard, R. Roca, N. Viltard, M. Viollier, and N. Karouche (2007), Megha-Tropiques : un satellite hydrométéorologique franco-indien, La Météorologie, 57, 19-27, DOI:10.4267/2042/18185.

Emde, C., S. A. Buehler, C. Davis, P. Eriksson, T. R. Sreerekha, and C. Teichmann (2004), A polarized discrete ordinate scattering model for simulations of limb and nadir long-wave measurements in 1-D/3-D spherical atmospheres, J. Geophys. Res., 109, D24207, doi:10.1029/2004JD005140.

English, S. J., and T. J. Hewison (1998). Fast generic millimeter-wave emissivity model. In: Asia-Pacific Symposium on Remote Sensing of the Atmosphere, Environment, and Space. International Society for Optics and Photonics, pp. 282-300.

Eriksson, P., S. A. Buehler, C. P. Davis, C. Emde, and O. Lemke (2011), ARTS, the atmospheric radiative transfer simulator, Version 2, J. Quant. Spectrosc. Radiat. Transfer, 112, 1551–1558.

Evans, K. F., J. R. Wang, P. E. Racette, G. Heymsfield, and L. Li (2005), Ice cloud retrievals and analysis with the compact scanning submillimeter imaging radiometer and the cloud radar system during CRYSTAL-FACE, J. Appl. Meteorol., 44, 839 – 859.

Galligani, V. S, C. Prigent, E. Defer, C. Jimenez, and P. Eriksson (2013), The impact of the melting layer on the passive microwave cloud scattering signal observed from satellites: A study using TRMM microwave passive and active measurements J. Geophys. Res., 118,

D05667, doi: 10.1002/jgrd.50431.

Goldstein, C., and N. Karouche (2013), CAL/VAL MADRAS Radiometric Sensitivity, report MAD_RAD_02 TRO-NT-32-NT-2817- CNES, 8 pages, available at http://smsc.cnes.fr/MEGHAT/PDF/MADRASRadiometricSensitivity.pdf.

Grody, N.C. (1991), Classification of snow cover and precipitation using the Special Sensor Microwave/Imager (SSM/I), J. of Geophys. Res., 96, 7423-7435.

Iguchi, T., T. Kozu, R. Meneghini, J. Awaka, and K. Okamoto (2000), Rain-profiling algorithm for the TRMM precipitation radar, J. Appl. Meteor., 39, 2038–2052.

Jimenez, C., S. A. Buehler, B. Rydberg, P. Eriksson and K. F. Evans (2007), Performance simulations for a submillimetre-wave cloud ice satellite instrument, Q. J. R. Meteorol. Soc., 133, 129-149.

Karouche, N., A. Rosack, C. Golstein, J. Rollin, B. Picart, E. Hillairet, S. Chowdhury, and D. K. Jain (2013), Megha-Tropiques L1 product definition, TRO-0-ST-1610-CNES, available at http://smsc.cnes.fr/MEGHAT/PDF/2013_01_17_Level-1productdef_ED3rev4.pdf.

Karouche, N., C. Goldstein, A. Rosak, C. Malassingne, and G. Raju (2012), Megha-Tropiques Satellite Mission : In Flight Performances Results, Geoscience and Remote Sensing Symposium (IGARSS), 2012 IEEE International, 4684-4687, 10.1109/IGARSS.2012.6350420.

Karouche, N., and G. Raju (2010), Megha-Tropiques Satellite Mission: Sensors performances, Proc. SPIE 7826, Sensors, Systems, and Next-Generation Satellites XIV, 78260Q (October 13, 2010), doi:10.1117/12.868048.

Kulie, M. S., R. Bennartz, T. J. Greenwald, Y. Chen, and F. Weng (2010), Uncertainties in Microwave Properties of Frozen Precipitation: Implications for Remote Sensing and Data Assimilation, J. Atmos. Sci., 67, 3471–3487.

Kummerow, C. D., S. Ringerud, J. Crook, D. Randel, and W. Berg (2011), An Observationally Generated A Priori Database for Microwave Rainfall Retrievals. J. Atmos. Oceanic Technol., 28, 113–130.

Kummerow, C., W. Barnes, T. Kozu, J. Shiue, and J. Simpson (1998), The tropical rainfall measuring mission (TRMM) sensor package, J. Atmos. Oceanic Technol., 15, 809–817.

Lafore, J.-P., J. Stein, N. Asencio, P. Bougeault, V. Ducrocq, J. Duron, C. Fischer, P. Héreil, P. Mascart, V. Masson, J.-P. Pinty, J.-L. Redelsperger, E. Richard, and J. Vilà-Guerau de Arellano (1998) ; The Meso–NH Atmospheric Simulation System. Part I: adiabatic formulation and control simulations. Scientific objectives and experimental design. Ann. Geophys., 16, 90–109.

Liebe, H. J., G. A. Huord, and T. Manabe (1991), A model for the complex permittivity of water at frequencies below 1 THz, International Journal of Infrared and Millimeter Waves, 12 (7).

Liu, G. (2004), Approximation of single scattering properties of ice and snow particles for high microwave frequencies, Journal of the atmospheric sciences 61 (20), 2441–2456.

Matrosov, S. Y., A. J. Heymsfield, and Z. Wang (2005), Dual-frequency radar ratio of nonspherical atmospheric hydrometeors, Geophys. Res. Lett., 32, L13816, doi:10.1029/2005GL023210.

Matzler, C., P.W. Rosenkranz, A. Battaglia and J.P. Wigneron (2006), Thermal Microwave Radiation - Applications for Remote Sensing, IEE Electromagnetic Waves Series 52, London, UK, Chapter 5.

Meirold-Mautner, I., C. Prigent, E. Defer, J.-R. Pardo, J.-P. Chaboureau, J.-P. Pinty, M. Mech, and S. Crewell (2007), Radiative transfer simulations using mesoscale cloud model outputs: comparisons with passive microwave and infrared satellite observations for mid-

latitudes, J. Atmos. Sci., 64, 1550-1568.

Miao, J., K.-P. Johnsen, S. Buehler, and A. Kokhanovsky (2003), The potential of polarization measurements from space at mm and sub-mm wavelengths for determining cirrus cloud parameters, Atmospheric Chemistry and Physics 3 (1), 39–48.

Mishchenko, M. I. (2000), Calculation of the amplitude matrix for a non spherical particle in a fixed orientation, Appl. Opt., 39, 1026–1031.

Olson, W.S., P. Bauer, N.F. Viltard, D.E. Johnson, W.-K. Tao, R. Meneghini, and L. Liao (2001a), A Melting-Layer Model for Passive/Active Microwave Remote Sensing Applications. Part I: Model Formulation and Comparison with Observations, J. Appl. Meteor., 40, 1145–1163.

Olson, William S., P. Bauer, C. D. Kummerow, Y. Hong, and W.-K. Tao (2001b), A Melting-Layer Model for Passive/Active Microwave Remote Sensing Applications. Part II: Simulation of TRMM Observations, Journal of Applied Meteorology 40, 1164–1179.

Prigent, C., E. Defer, J. Pardo, C. Pearl, W. B. Rossow, and J.-P. Pinty (2005), Relations of polarized scattering signatures observed by the TRMM Microwave Instrument with electrical processes in cloud systems, Geophys. Res. Let., 32, L04810, doi: 10.1029/2004GL022225.

Prigent, C., J. R. Pardo, M. I. Mishchenko and W. B. Rossow, Microwave polarized scattering signatures in clouds: SSM/I observations interpreted with radiative transfer simulations, Journal of Geophysical Research, 106, 28243-28258, 2001.

Sekhon, R. S., and R. C. Srivastava (1970), Snow size spectra and radar reflectivity, J. Atmos. Sci., 27, 299–307.

Stubenrauch, C. J., W. B. Rossow, S. Kinne, S. Ackerman, G. Cesana, H. Chepfer, L. Di Girolamo, B. Getzewich, A. Guignard, A. Heidinger, B. C. Maddux, W. P. Menzel, P.

Minnis, C. Pearl, S. Platnick, C. Poulsen, J. Riedi, S. Sun-Mack, A. Walther, D. Winker, S. Zeng, G. Zhao (2013), Assessment of Global Cloud Datasets from Satellites: Project and Database Initiated by the GEWEX Radiation Panel, Bulletin of the American Meteorological Society 94:7, 1031-1049.

Surussavadee, C., and D. H. Staelin (2006), Comparison of AMSU millimeter-wave satellite observations, MM5/TBSCAT predicted radiances, and electromagnetic models for hydrometeors, IEEE Trans. Geo. Remote Sens., 44, 2667–2678.

Wiedner, M., C. Prigent, J. R. Pardo, O. Nuissier, J.-P. Chaboureau, J.-P. Pinty, and P. Mascart (2004), Modeling of passive microwave responses in convective situations using output from mesoscale models: Comparison with TRMM/TMI satellite observations, J. Geophys. Res., 109, D06214, doi:10.1029/2003JD004280.

Xie, X., U. Lohnert, S. Kneifel, and S. Crewell (2012), Snow particle orientation observed by ground-based microwave radiometry, J. Geophys. Res., 117, D02206, doi:10.1029/2011JD016369.

Xie, X., and J. Miao (2011), Polarization difference due to non randomly oriented ice particles at millimeter/submillimeter waveband, J. Quant. Spectrosc. Ra., 112, 1090–1098.

Table 1. Characteristics of the MADRAS instrument on board Megha-Tropiques. Different

radiometric sensitivities are given: the specification ones (Goal and Required) and the in-

flight and ground estimates from CNES at nominal MADRAS operations [Karouche et al.,

2012; Goldstein and Karouche, 2013]. NEDT stands for Noise Equivalent Differential

Temperature.

Central frequency (GHz)	Bandwidth (GHz)	Pol.	Cross track resolution (km)	Along track resolution (km)	NEDT (K) Goal	NEDT (K) Req'd	NEDT (K) Flight	NEDT (K) Ground
18.7	±0.1	H	40	67	0.5	0.7	0.33	0.37
18.7	±0.1	V	40	67	0.5	0.7	0.38	0.44
23.8	±0.2	V	40	67	0.5	0.7	0.34	0.39
36.5	±0.5	H	40	67	0.5	0.7	0.28	0.32
36.5	±0.5	V	40	67	0.5	0.7	0.28	0.33
89	±1.35	H	10	17	1	1.1	0.38	0.41
89	±1.35	V	10	17	1	1.1	0.36	0.39
157	±1.35	H	6	10	2	2.6	1.01	1.08
157	±1.35	V	6	10	2	2.6	0,94	1.08
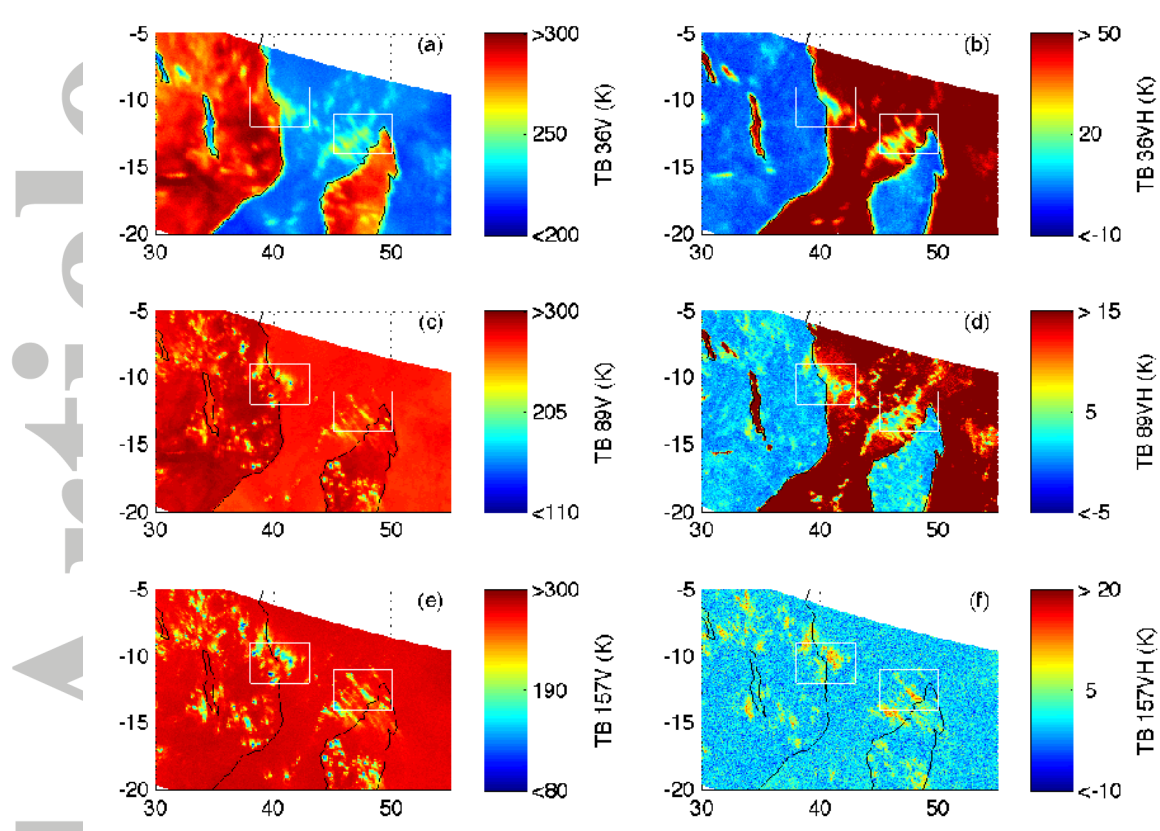
Figure 1 - A scene from MADRAS on board Megha-Tropiques, off the east coast of Africa, on December 9th, 2011, between 12:05 and 12:12 TU. From top to bottom, 36, 89, and 157 GHz, on the left the vertical polarization, on the right the difference between vertical and horizontal polarizations (TBVH). The two regions plotted in Figure 2 and Figure 3 are also indicated.
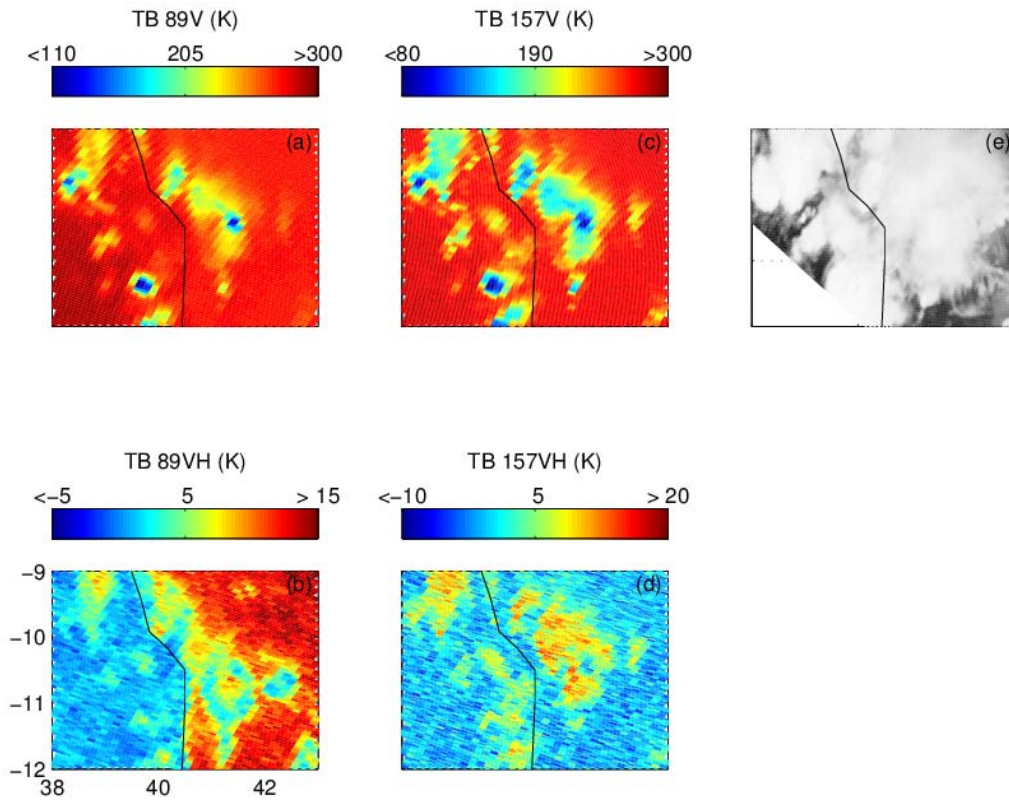
Figure 2 – Zoom on one area of Figure 1 with (a) TB89V map, (b) TB89VH map, (c) TB157V map, (d) TB157VH map, (e) almost time-coincident (see Annex) TRMM VIRS 12-μm IR image.
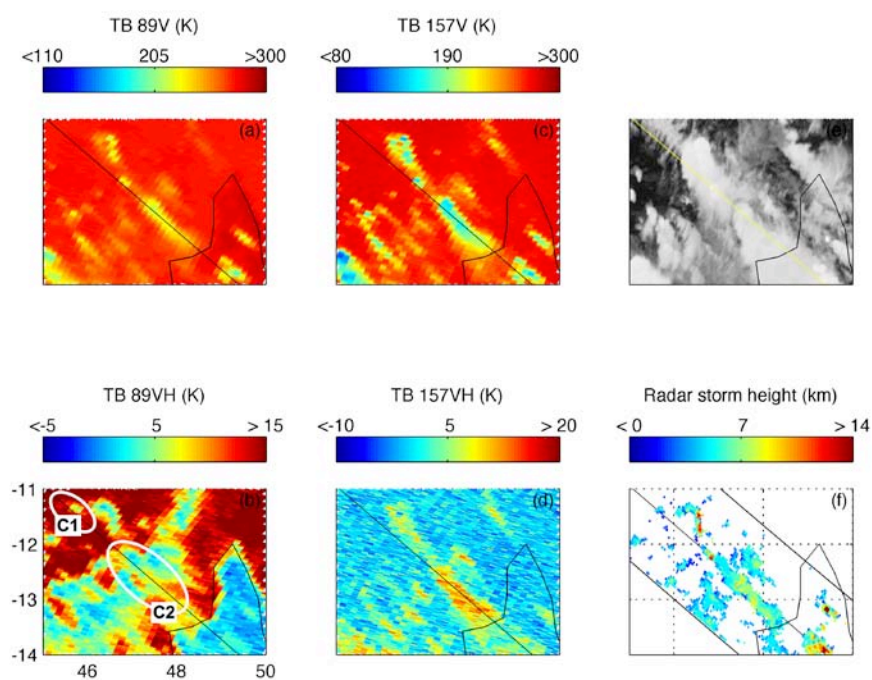
Figure 3 – Same as Figure 2 but for another region with in addition (f) almost time-coincident TRMM PR storm height. The solid lines in (f) delineate the borders of the PR swath. The yellow line in (e) and the black line in the other panels locate the transect of interest used in Section 3.3. C1 and C2 indicate the regions of interest investigated in Section 3.3.
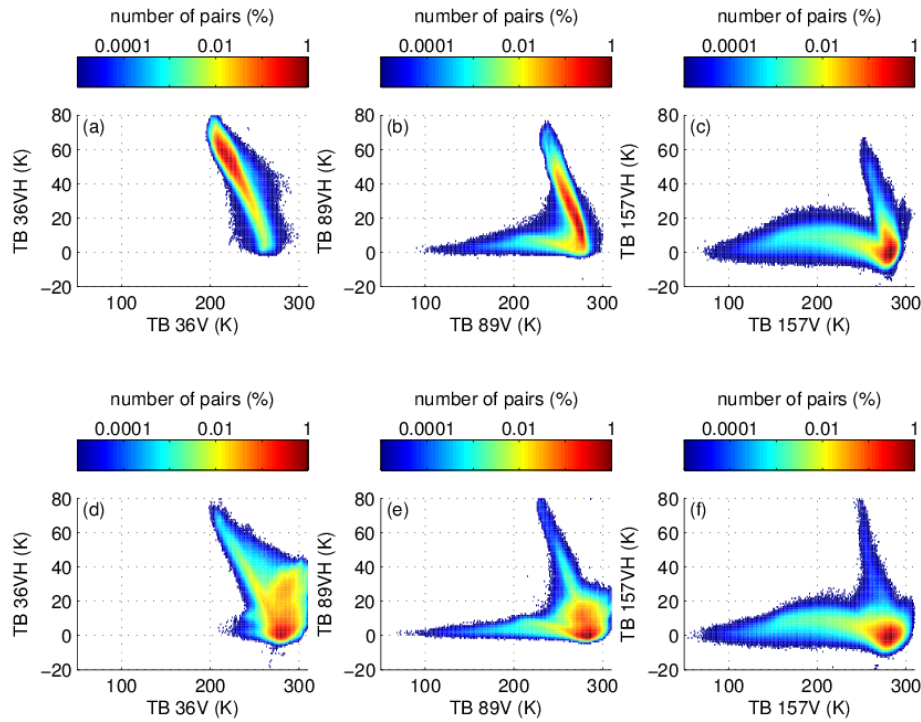
Figure 4 - The brightness temperature polarization differences (TBVH) versus the brightness temperature in vertical polarization (TBV), for ocean (top) and land (bottom), for 36, 89, and 157 GHz from left to right. For each 1 K by 1 K box, the color indicates the relative number of TBV-TBVH pairs, with respect to the total number of TBV-TBVH pairs considered in the analysis. More than 235 (80) millions of observations at157 GHz were used over ocean (land). The number of samples at 36 and 89 GHz is about half the number of 157 GHz samples.
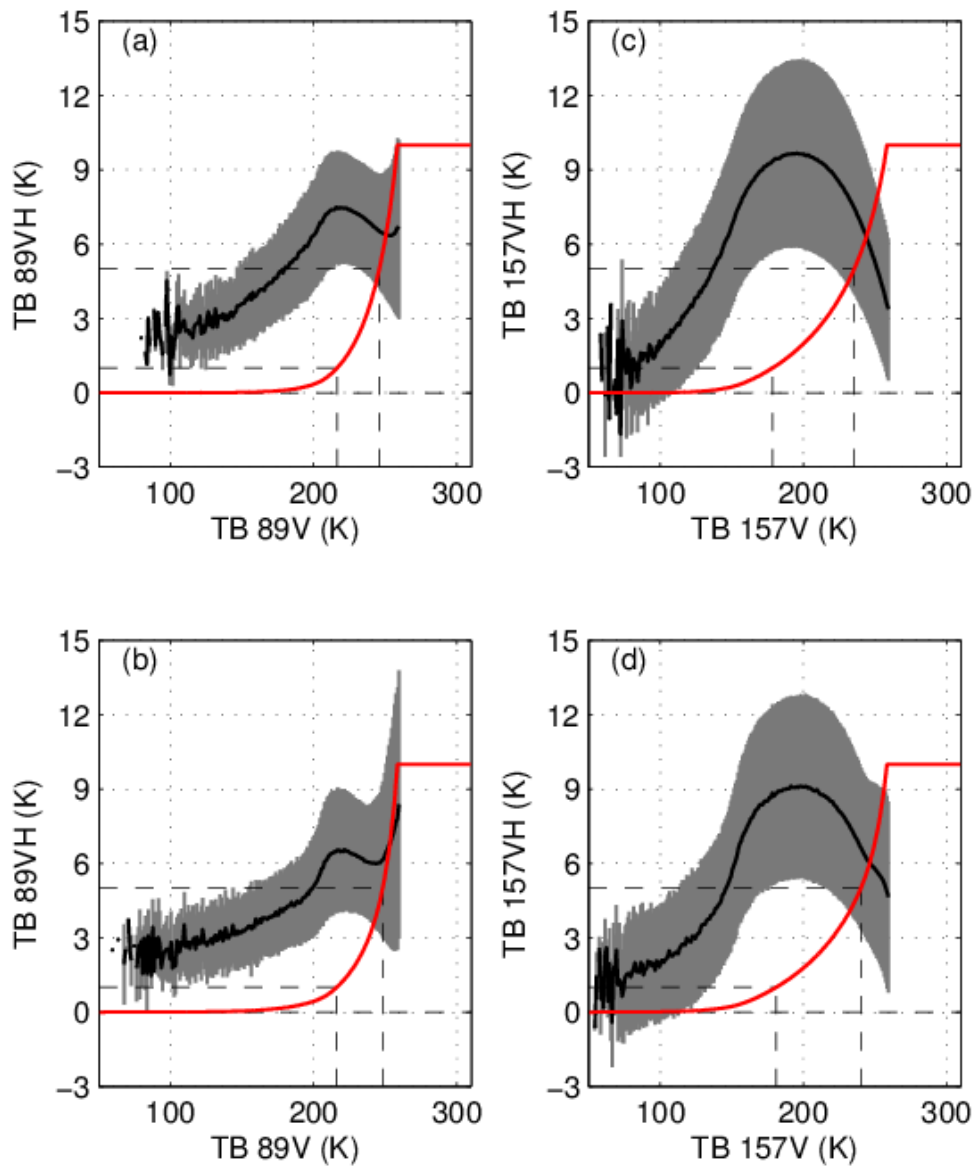
Figure 5 - Most probable polarization difference (solid black lines) and its standard deviation (in grey) at 89 and 157 GHz for ocean (top) and land (bottom) in the scattering regime (see text for the methodology to identify the scattering regime). The red curve shows the cumulative distribution of the number of samples (rescaled between 0 and 10 K) with the dashed lines corresponding to 0, 10 and 50% of the sample population in the scattering regime.
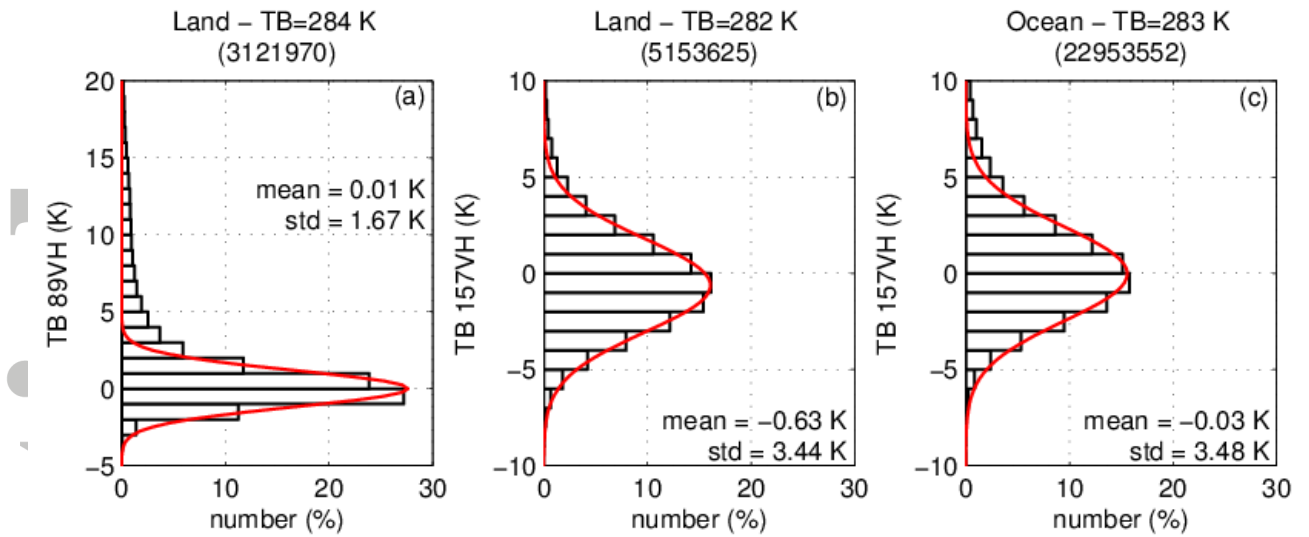
Figure 6 - Distribution of the polarization difference at the maximum of the distributions shown in Figure 4 over land at 89 and 157 GHz (a, b) and over ocean at 157 GHz (c). The brightness temperature that corresponds to the maximum is given at the top of each panel as well as the number of TBV-TBVH pairs with that maximum brightness temperature.
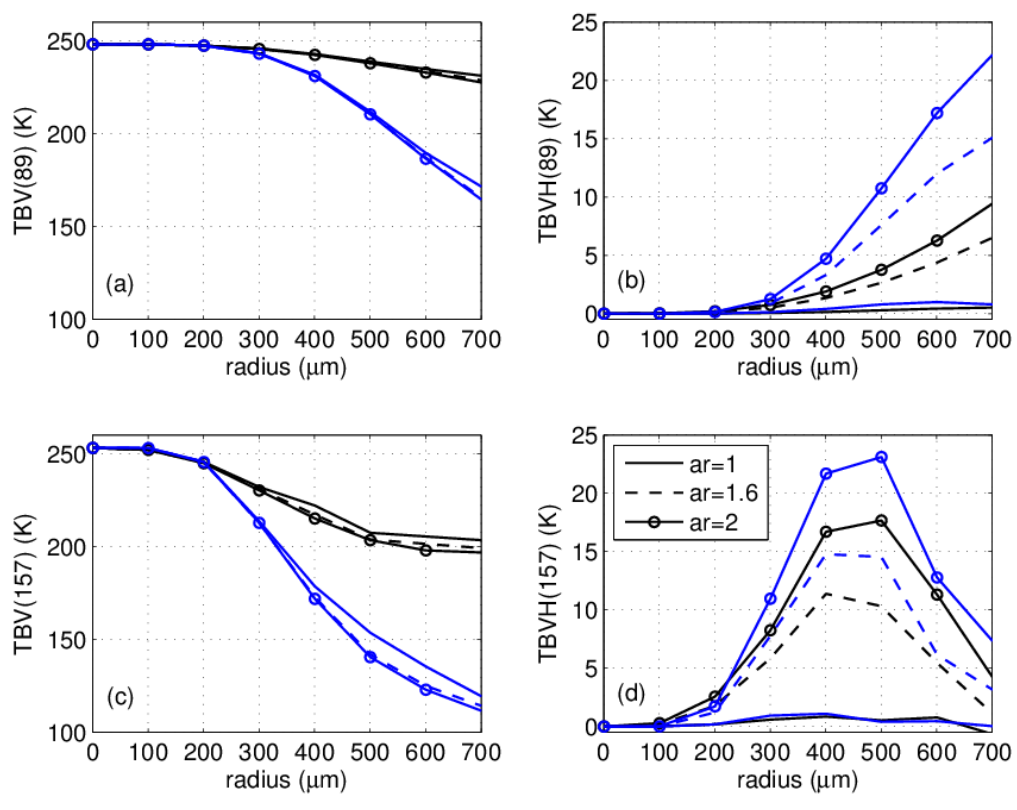
Figure 7 - The sensitivity of the vertical brightness temperature (TBV) and the polarization difference (TBVH) at 89 GHz and 157 GHz to the particle aspect ratio as a function of the effective radius for a mono disperse distribution of pure ice (black) and dry snow (blue) horizontally aligned spheroids (fixed IWP at 0.2 kg/m^2). The parameter "*ar*" stands for aspect ratio and corresponds to the ratio of the longest to the shortest axis of the spheroids.
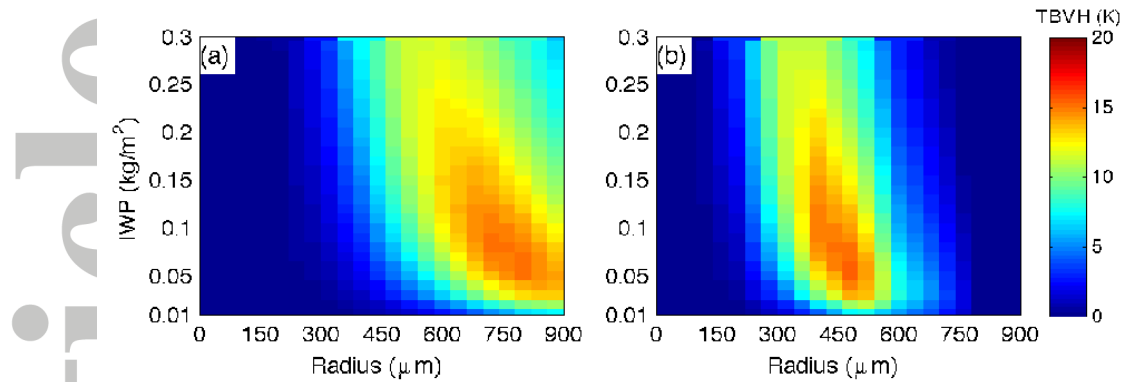
Figure 8 - The sensitivity of the polarization difference (TBVH) at (a) 89 GHz and (b) 157 GHz for a mono-disperse distribution of dry snow horizontally aligned spheroids, as a function of the IWP and as a function of the particle (effective) radius.
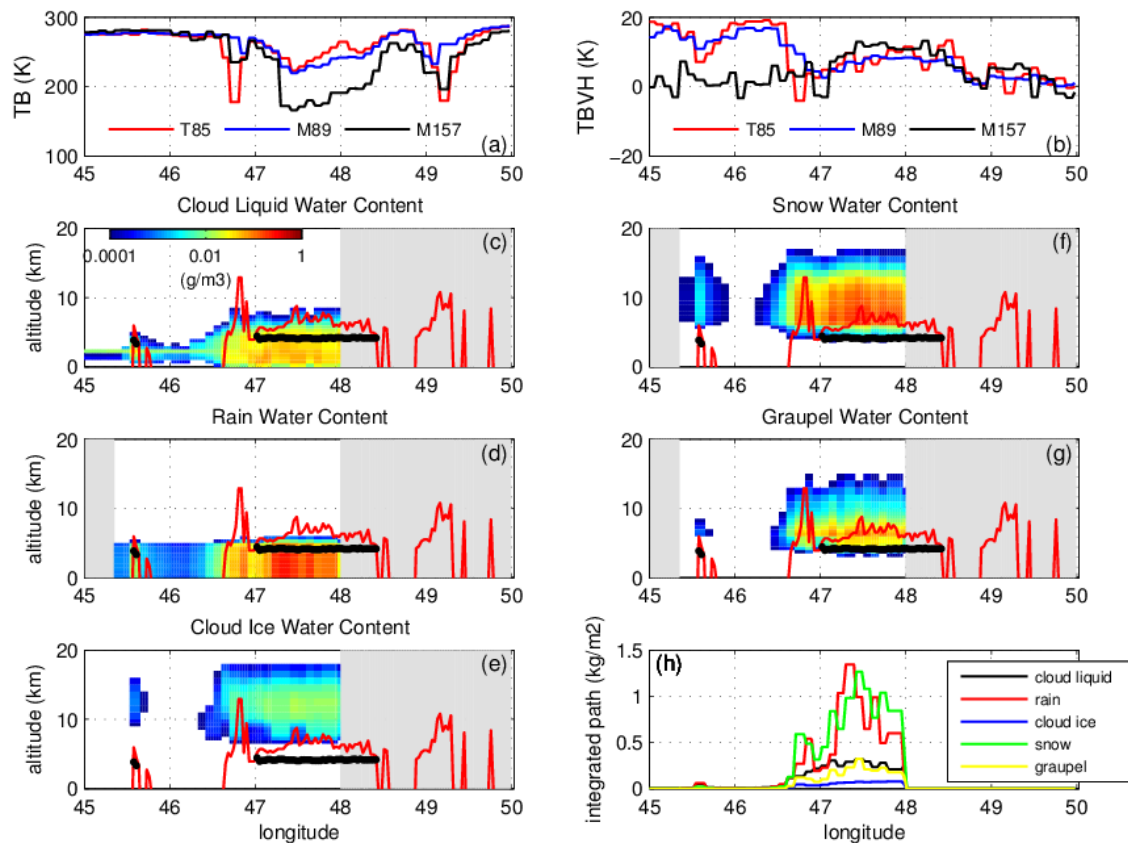
Figure 9 – Brightness temperatures and the retrieved v7 TMI 2A12 hydrometeor profiles along the transect of interest: (a) TMI 85 GHz (T85) TBV and MADRAS 89 GHz (M89) and 157 GHz (M157) TBV, (b) TMI 85 GHz TBVH and MADRAS 89 GHz and 157 GHz TBVH, (c) the cloud liquid water content (CWC), (d) the rain water content (RWC), (e) the cloud ice water content (IWC), (f) the snow water content (SWC), (g) the graupel water content (GWC), and (h) the hydrometeor integrated paths. Note that the PR bright band height (black dots) and the PR cloud top height (solid red curve) are overlaid, while 2A12 TMI profiles with bad quality flag are plotted in grey. TMI 2A12 retrieval is not available over land (east of 48E).
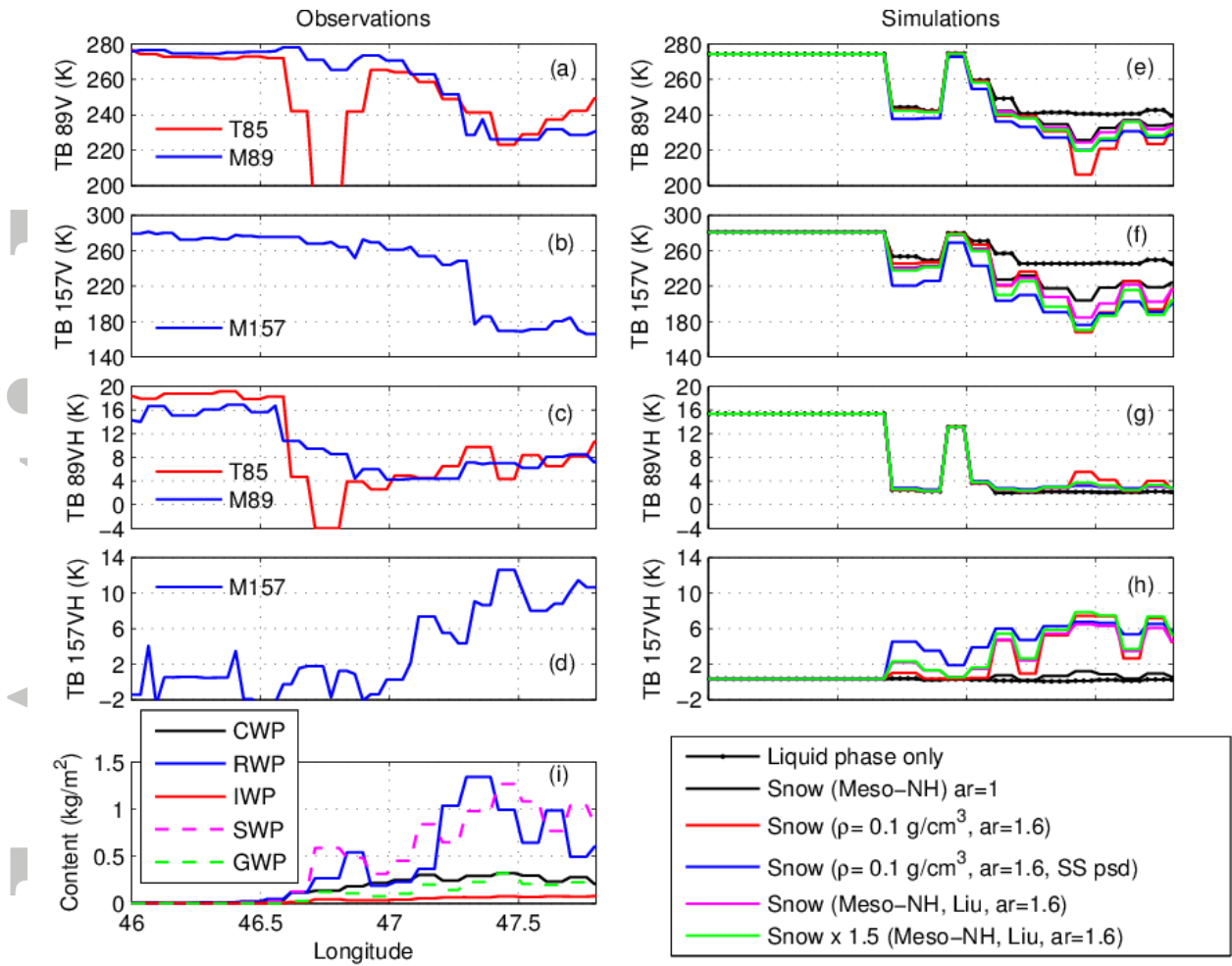
Figure 10 - The TBV and TBVH signals at 89 and 157 GHz observed by MADRAS

including TMI 85 GHz records (left), and simulated with ARTS (right) under different

microphysical properties of dry snow species, for the transect of interest. In (i) CWP, RWP,

IWP, SWP and GWP stand for cloud water path, rain water path, ice water path, snow water
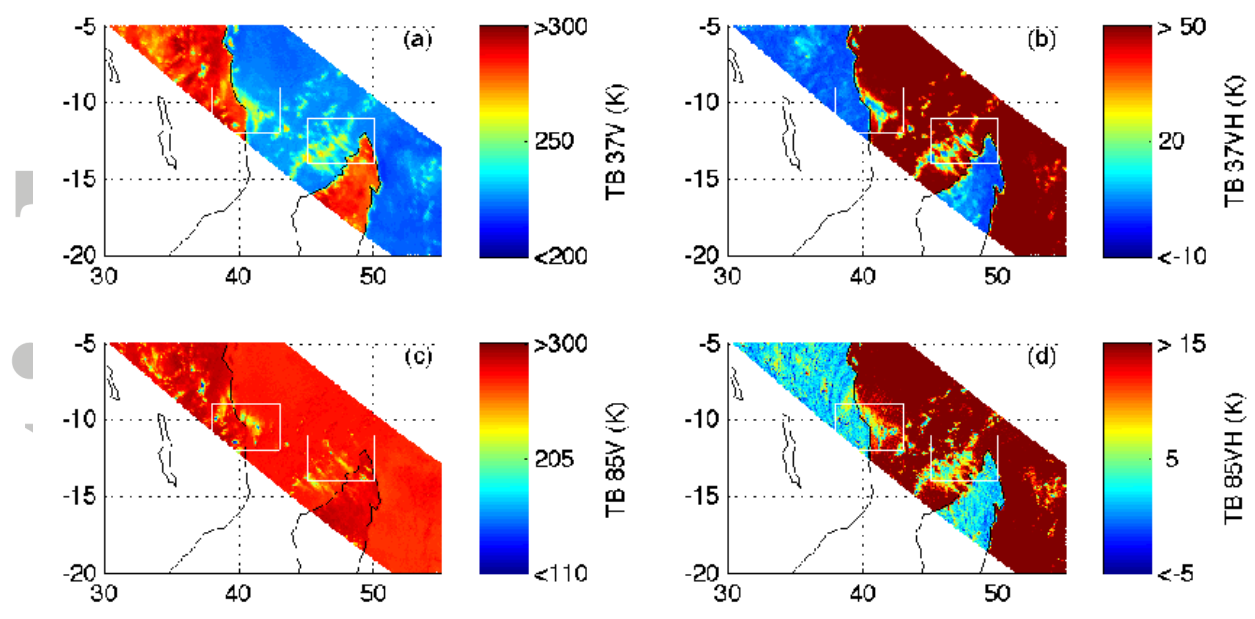
path and ice water path respectively.

Figure A.1 - Same as Figure 1 but with TMI records for the period 12:10-12:18 UT on December 9th, 2011.
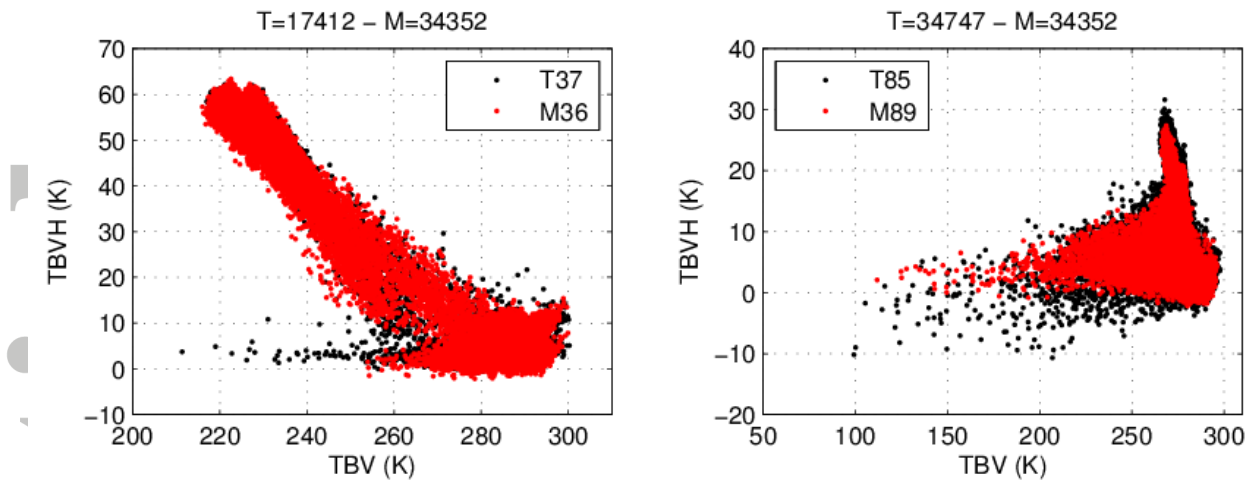
Figure A.2 - Scatter plots of brightness temperatures and polarization differences at the studied bands for the two instruments for ocean and land beams together for the common area delineated by the intersections of MADRAS and TMI swaths shown in Figure 1 and Figure A1. T and M stand for TMI and MADRAS respectively.
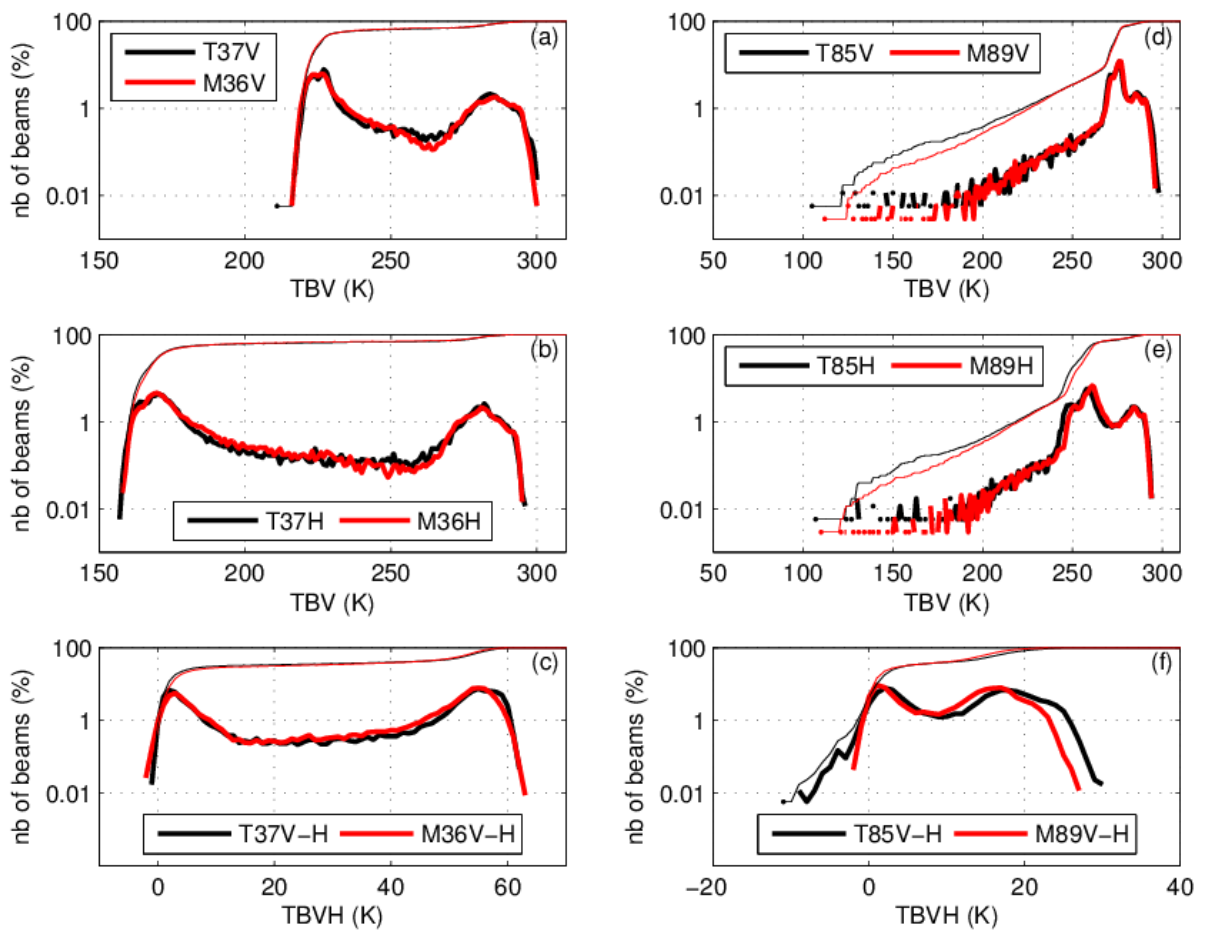
Figure A.3 - Histograms (in solid lines) and cumulative distributions (in thin lines) of the brightness temperatures mapped in Figures 1 and A.1 for common radiometric bands. Only beams located within the common area defined by the intersections of the overpasses of the two swaths were used to produce the plot. T and M stand for TMI and MADRAS respectively.